

***Final Draft***  
**of the original manuscript:**

Kashaev, N.; Pugachev, D.; Ventzke, V.; Fomin, F.; Burkhardt, I.; Enz, J.;  
Riekehr, S.:

**Microstructure and mechanical performance of autogenously  
fibre laser beam welded Ti-6242 butt joints**

In: Materials Science and Engineering A (2017) Elsevier

DOI: 10.1016/j.msea.2017.03.115

## **Microstructure and mechanical performance of autogenously fibre laser beam welded Ti-6242 butt joints**

Nikolai Kashaev, Dmitry Pugachev, Volker Ventzke, Fedor Fomin,  
Irmela Burkhardt, Josephin Enz, Stefan Riekehr

Institute of Materials Research, Materials Mechanics,  
Helmholtz-Zentrum Geesthacht,  
Max-Planck-Str.1, 21502 Geesthacht, Germany

Corresponding author: Nikolai Kashaev, [nikolai.kashaev@hzg.de](mailto:nikolai.kashaev@hzg.de)

### **Highlights:**

- Autogenous fibre LBW of Ti-6242 was successfully achieved
- Butt joints showed low levels of porosity and an appropriate seam geometry
- Base material level of strength achieved for tensile strength
- Predicted critical underfill depth is 25% of the specimen thickness

### **Abstract:**

This work deals with the effects of laser beam power, focus position and advance speed on the geometry, microstructure and mechanical properties such as the tensile strength and microhardness of autogenously fibre laser beam welded Ti-6Al-2Sn-4Zr-2Mo (denoted as Ti-6242) butt joints used for high temperature applications. The Ti-6242 sheet employed here is characterized by a globular ( $\alpha + \beta$ ) microstructure. The heat input during laser beam welding led to the formation of a martensitic  $\alpha'$ -phase in the fusion zone. The heat affected zone consisted of globular grains and acicular crystallites. These local transformations were connected to a change in the micro-texture, average grain size and  $\beta$ -phase content. Furthermore, the microhardness increased from 330 HV 0.3 to 450 HV 0.3 due to the martensitic transformation. The mechanical behaviour of the laser beam welded Ti-6242 butt joint loaded in tension was determined by the properties of the

Ti-6242 base material. The local microhardness increase provided a shielding effect that protected the Ti-6242 butt joint against any mechanical damage. The predicted critical total underfill depth that does not reduce the tensile strength of the weld was determined to be 25% of the specimen thickness.

**Keywords:** laser beam welding; Ti-6242; butt joint; microstructure; tensile strength; finite element analysis.

## 1. Introduction

The ( $\alpha + \beta$ )-titanium alloy Ti-6Al-2Sn-4Zr-2Mo (referred to here as Ti-6242) was introduced in 1967 for high temperature applications in the high pressure compressor section of aero-engines, where the temperature exceeds 350 °C and the widely used titanium alloy Ti-6Al-4V cannot be applied because of creep considerations, as reported by (Davis, 1997). Besides typical applications, such as blades and discs, as reported in the work of (Lütjering & Williams, 2007), (Davis, 1997) describes applications in sheet-metal forming for engine afterburner structures and for various “hot” airframe skin applications. Thin Ti-6242 sheet structures cannot be easily joined by friction stir welding, as the high strength of Ti-6242 requires welding tools with excellent wear and corrosion resistance. However, fusion welding processes such as arc welding, electron beam welding and laser beam welding are suitable joining methods for Ti-6242 thin walled structures. The microstructure and mechanical performance of gas tungsten arc and laser beam welded Ti-6242 were studied by (Baeslack III & Banas, 1981). The authors presented defect-free and highly efficient Ti-6242 joints via the use of autogenous laser beam welding (LBW) with a 7 kW CO<sub>2</sub>-laser or gas tungsten arc welding (GTAW) process. The effect of post-weld heat treatment on the microstructure and mechanical properties of the weldments was also investigated in the above mentioned work. Ti-6242 joints with high ductility and base material (BM) level of strength have also been reported by (Torster, et al., 1999) for LBW of Ti-6242 with a 6.3 kW CO<sub>2</sub>-laser source and with an 8 kW fibre laser by the authors of this study (Kashaev, et al., 2016). A recent study of (Chamanfar, et al., 2016) presented lower ductility and strength values for

the weldments compared to those for the BM. Unfortunately, detailed information on the LBW process was not included. The reason for the inferior strength and ductility was explained by the presence of welding defects such as porosity and underfill in the fusion zone (FZ), as well as higher hardness in the FZ and the heat affected zone (HAZ) compared to the BM. In general, LBW of Ti-6242 can be performed without difficulties if attention is paid to weld preparation, cleaning and inert gas shielding, as mentioned by (Torster, et al., 1999). Little attention was paid in the literature to the influence of the LBW process parameters on the microstructure and mechanical performance of the welds. As a continuation of our previous study using an 8 kW fibre laser (Kashaev, et al., 2016), this study correlates the LBW process parameters with the geometry and microstructure of the welds. Special attention was also paid to determining acceptable welding defects such as underfill that will not reduce the overall tensile properties of the butt joints.

## **2. Experimental methods**

### **2.1. Material and laser beam welding**

Commercially available Ti-6242 sheet material with a thickness of 2.0 mm was used for the LBW experiments. The chemical composition of the raw material was determined by the energy dispersive X-ray analysis (EDX) and is listed in

Table 1. LBW of the butt joints was performed using an 8.0 kW fibre laser. Butt joints were welded autogenously in a 3-axis Ixion CNC machine. The welding direction was perpendicular to the rolling direction (longitudinal (L) direction) of the sheet specimens (Fig. 6(e)). Each specimen was clamped in a box open to the top, which was filled with an Ar shielding gas to protect the weld zone from ambient air during the LBW process. Before welding, the surface of the titanium sheets was cleaned using mechanical grinding followed by alcohol cleaning. The LBW process parameters investigated in this study are summarized in Table 2.

Table 1. Chemical composition (wt.%) of the investigated titanium alloy determined by EDX analysis.

<b>Ti</b>	<b>Al</b>	<b>Sn</b>	<b>Zr</b>	<b>Mo</b>
88.2	5.1	1.8	3.5	1.4

Table 2. Parameters of the LBW of butt joints.

<b>Parameters</b>	<b>Variation range</b>
<b>Laser power</b>	3.0 – 8.0 kW
<b>Fibre core diameter</b>	300 $\mu\text{m}$ (constant)
<b>Collimator length</b>	150 mm (constant)
<b>Focal length</b>	300 mm (constant)
<b>Focus spot diameter</b>	600 $\mu\text{m}$ (constant)
<b>Focus position above the surface</b>	0.0 – 10.0 mm
<b>Advance speed</b>	2.0 – 8.0 m/min
<b>Argon flow rate</b>	15 l/min (constant)

## 2.2. Microstructural characterization

The specimens for metallographic analysis were prepared by conventional procedures followed by a final vibration polishing with an oxide polish suspension compound (OPS). The specimens were etched prior to optical microscopy investigations to determine the geometrical features of the welds. Visual inspections were also used to analyse the outer appearance of the weld seams to examine for weld imperfections, e.g., underfill, undercut, spatter and excess of penetration. The X-ray inspections were used to determine any inner imperfections in the welds, including porosity and cracks.

The microstructures of the laser beam welded Ti-6242 butt joints were also investigated using scanning electron microscopy (Jeol JSM-6490LV) with electron back-scatter diffraction (EBSD) (EDAX TSL OIM) to determine the local micro-texture, phase contents and grain sizes within the BM, HAZ and FZ to examine any local changes caused by the thermal cycle associated with the welding process. The EBSD

measurements were performed at 30 kV, an emission current of 75  $\mu$ A, a sample tilt angle of 70  $^{\circ}$ , a working distance of 14 mm, a magnification of 750x and a step size of 0.5  $\mu$ m. The scan field size was fixed at 125  $\mu$ m  $\times$  125  $\mu$ m. The orientation calculation was based on the GSHE method, where triclinic sample symmetry could be assumed. The metallographic samples used for EBSD analysis and microhardness testing were prepared by conventional multi-stage grinding and subsequent electrolytic polishing (60% HClO<sub>4</sub> (60 ml) + (methanol + 2-butoxy-ethanol) (1000 ml)). Maps and recalculated inverse pole figures were used to illustrate the microstructure crystal orientations. The colours in the crystal orientation maps are based on the corresponding colour-coded inverse pole figure. The basal  $\langle 0\ 0\ 0\ 1 \rangle$  crystal direction parallel to the surface normal direction ND = [001] is red, the prismatic  $\langle 1\ 0\ -1\ 0 \rangle$  crystal direction is blue, and the prismatic  $\langle 2\ -1\ -1\ 0 \rangle$  crystal direction is green. Intermediate directions are characterized by corresponding intermediate colours.

### **2.3. Mechanical testing**

Microhardness profiles across the joint were obtained using an automated Vickers hardness testing machine with a 0.3 kg load. Standard tensile tests were performed at ambient temperature according to the DIN EN ISO 6892-1:2009 standard. The load-bearing cross section of the tensile specimen was 12.5 mm  $\times$  2.0 mm, and the total specimen length was 165 mm. A 100 kN electro-mechanical universal testing machine with a constant transverse main displacement was used. The elongation of the specimen was measured with a laser extensometer with an initial length,  $l_0$ , of 50 mm. For the welded specimen, the weld was always located exactly in the middle of  $l_0$ .

### **3. Results and Discussion**

#### **3.1 Macroscopic appearance of the welds**

Butt joints with different seam shapes were obtained using a wide process parameter range, as summarized in Table 2. Typical morphologies of the Ti-6242 butt joints are represented in the cross sections shown in Fig. 1(a)-(d). The present macrographs show that the weld shapes are strongly dependent on the LBW parameters. For this purpose, the linear heat input (kJ/m) is defined as the quotient from the laser beam power (kW) and the advance speed (m/s) and was used to describe the effects of the process parameter variations on the seam shape development. The values of the linear heat input are also shown in Fig. 1.

Ti-6242 butt joints with full penetration can already be achieved at linear heat inputs higher than 22.5 kJ/m. The image series in Fig. 1(a)-(c) shows that the size of the weld seam increases with the linear heat input. The appearance of the larger weld seam in Fig. 1(b) is caused by near heat conduction welding. (Cao, et al., 2014) investigated Nd:YAG laser beam welding of Ti-6Al-4V and found that as the linear heat input increased, the weld seam geometry evolves from an hourglass morphology to a wide, nearly rectangular shape. Moreover, a change in the welding mode takes place, transitioning from the keyhole to the heat conduction mode. For linear heat inputs between 90 kJ/m and 240 kJ/m, the LBW process for Ti-6242 at lower advance speeds is situated between the keyhole and heat conductive modes. It is not possible to clearly distinguish these two welding modes.

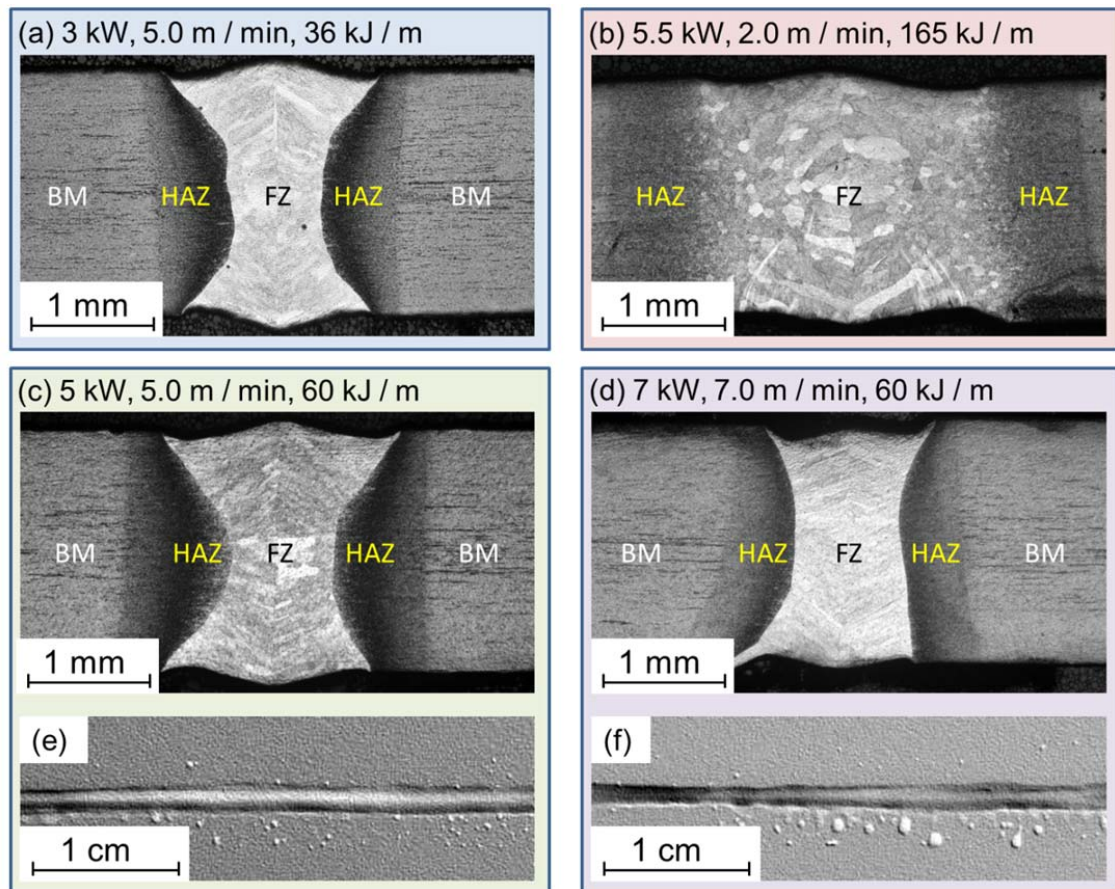


Fig. 1. Macrographs of Ti-6242 butt joints welded at (a) 3 kW laser power with 5.0 m/min advance speed, (b) 5.5 kW laser power with 2.0 m/min advance speed, (c) 5 kW laser power with 5.0 m/min advance speed, (d) 7 kW laser power with 7.0 m/min advance speed, and radiographs of the (e) butt joint welded at 5 kW laser power with 5.0 m/min advance speed and (f) 7 kW laser power with 7.0 m/min advance speed.

Fig. 1(c) and (d) show cross sections of the Ti-6242 butt joints welded with different combinations of laser beam power and advance speed, which results in the same linear heat input of 60 kJ/m but different seam shapes. Butt joint welding at a laser beam power of 5.0 kW and an advance speed of 5.0 m/min leads to the formation of hourglass shape, whereas laser beam welding at 7.0 kW and 7.0 m/min tends to form an I-shape. From this, it follows that the combination of the laser power and advance speed exerts a significant influence on the evolution of the weld seam shape.

The butt joints welded at a laser power of 5.0 kW and an advance speed of 5.0 m/min exhibit a uniform shape along the whole weld line with lower spatter level but without severe undercuts and underfills (Fig. 1(e)). In contrast to the butt joint in Fig. 1(c), the butt joint welded at a higher laser power combined with higher advance speed (Fig. 1(d)) exhibits larger underfills (Fig. 1(f)), which are caused by expulsion of the welded material. All of the butt joints exhibit low levels of defects such as porosity, cracks and impurities.

(Squillace, et al., 2012) analysed the influence of the LBW process parameters on the FZ and HAZ widths measured at the middle of the weld for autogenous LBW of Ti-6Al-4V using a Nd:YAG laser. For autogenous LBW using a 2.0 kW Nd:YAG-laser, the FZ and HAZ widths were found to be well correlated to the linear heat input. The results from (Squillace, et al., 2012) were also in good agreement with the results obtained for LBW of Ti-6Al-4V with a filler wire using a 3.3 kW Nd:YAG laser (Kashaev, et al., 2016). However, for LBW of Ti-6242 using a fibre laser at a higher power, the correlation of weld geometry characteristics such as the HAZ and FZ widths vs. linear heat input exhibited a noticeable scatter of the experimentally obtained values, as reported in our previous study (Kashaev, et al., 2016).

Fig. 1(c) and (d) clearly show that the weld seam morphology is not dependent solely on the linear heat input. For this reason, the dependence of the HAZ and FZ widths on the linear heat input (for the keyhole mode welding) was analysed at different laser power levels. The widths of the HAZ and the FZ were measured in the cross-sections of the butt joints at three different positions: radiation exposure side (RES), middle of the weld (M) and weld root side (WRS). A mean value of the HAZ width was calculated from the left and right HAZ, with the results shown in Fig. 2.

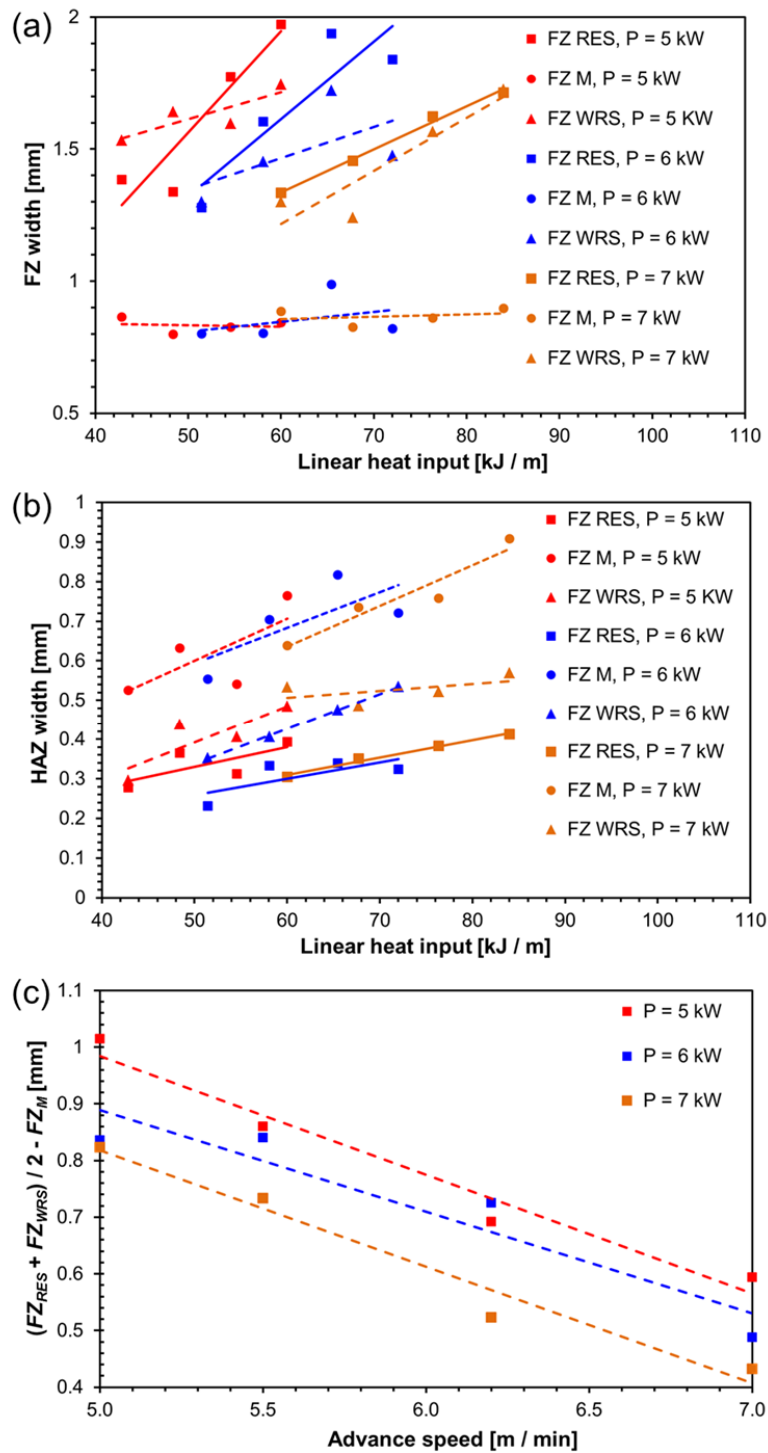


Fig. 2. (a) HAZ width, (b) FZ width vs. linear heat input for butt-joints welded at different laser power levels and (c) difference between the mean value of the FZ width for the RES and WRS and the FZ widths in the middle of the weld vs. advance speed for the three laser power levels.

The FZ width measured in the middle of the butt joint is nearly constant for the investigated parameter range. The width of the FZ measured at the RES and the WRS increases with the linear heat input for each investigated laser power level (Fig. 2(a)). The same trend was observed for the HAZ width, which was also measured in the middle of the weld (Fig. 2(b)). Fig. 2(c) shows the difference between the mean value of the FZ width for the RES and WRS and the FZ width in the middle of the weld vs. the advance speed for the three laser power levels denoted as parameter  $FZ_D$  and calculated according to the equation:

$$FZ_D = \frac{FZ_{RES} + FZ_{WRS}}{2} - FZ_M. \quad (1)$$

For each laser power level the relationship between the parameter  $FZ_D$  and the advance speed shows that as the advance speed increases, the parameter  $FZ_D$  decreases and vice versa. The parameter  $FZ_D$  is close to zero for a corresponding combination of high advance speeds and laser beam powers for full penetration, where the seam of the butt joint exhibits an I-shape. Fig. 3(a) demonstrates that an I-shaped seam was achieved at 8 kW of laser beam power and 8 m/min of advance speed using an 8 kW fibre laser. This type of laser system generates a laser beam with a top-hat distribution of power density and a long Rayleigh length, which enables a stable keyhole with an almost constant diameter through the Ti-6242 sheet thickness.

However, the butt joints welded at the highest laser power combined with the highest advance speed can lead to the formation of larger underfills. In the case of the Ti-6242 butt joint represented in Fig. 3(a), the total underfill  $UF = d - h$  is 0.39 mm (Fig. 3(b)), which is equivalent to 19.5 % of the sheet thickness. The definition of the total underfill is shown in Fig. 3(b). The detrimental effect of underfill is that mechanical properties of butt joints can be reduced.

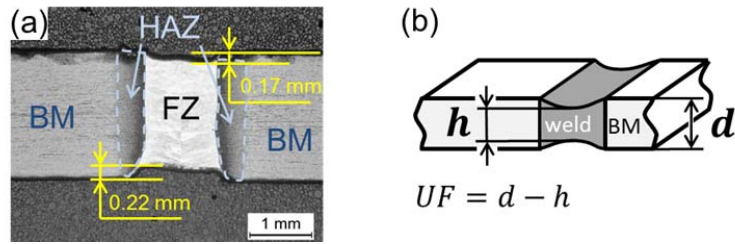


Fig. 3. (a) Macrographs of the butt joints welded at 8 kW laser power with 8.0 m/min advance speed and (b) a schematic representation of the butt joint for determination of the total underfill,  $UF$ .

### 3.2 Microstructure of laser beam welded Ti-6242 butt joints

The  $(0\ 0\ 0\ 1)_\alpha$  pole figure shown in Fig. 4(a) indicates that the Ti-6242 sheet was cross rolled. The  $\alpha$ -phase texture reveals basal poles of high intensity along the transverse direction TD and basal poles of lower intensity along the reference direction RD (rolling direction of the titanium sheet, Fig. 4(b)) with a wide spread angle of approximately  $80^\circ$ . This angle spreading is represented by an orientation band from  $(0\ 1\ -1\ 0)[2\ -1\ -1\ 0]$  at  $(0^\circ/90^\circ/0^\circ)$  to  $(0\ 1\ -1\ 0)[-2\ 1\ 1\ 0]$  at  $(180^\circ/90^\circ/0^\circ)$  in the ODF section at  $\varphi_2 = 0^\circ$ . Further micro-texture components are  $(0\ 0\ 0\ 1)[2\ -1\ -1\ 0]$  and  $(0\ 1\ -1\ 0)[0\ 0\ 0\ 1]$ . (Wood, et al., 1998) reported that cross-rolling is generally applied to reduce anisotropy.

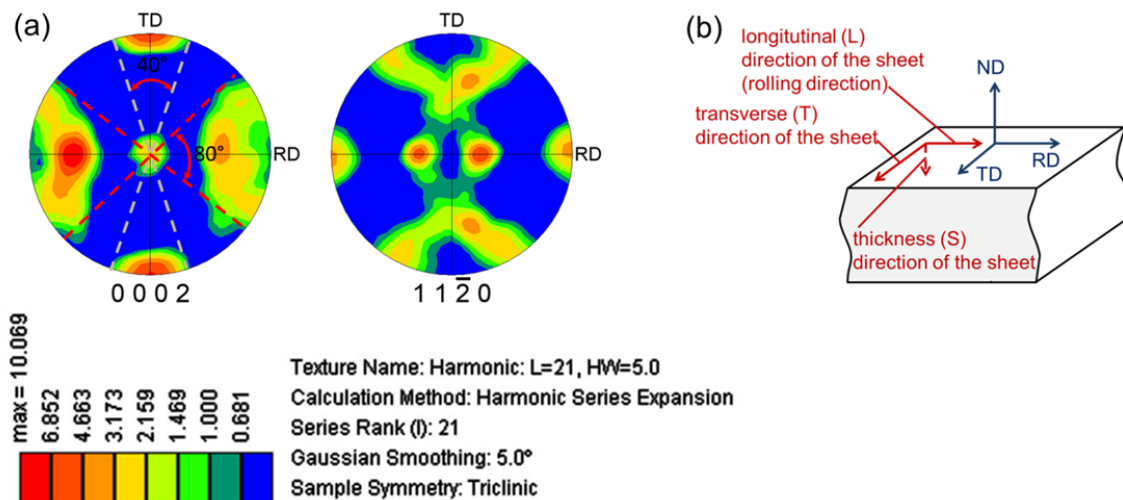


Fig. 4. (a) Initial  $\alpha$ -phase texture of the Ti-6242 sheet used for LBW trials in this work and (b) position of the coordinate system for the EBSD-analysis of the Ti-6242 sheet

specimen. The pole figure plane is the rolling plane of the sheet material, the reference direction (RD) is parallel to the rolling (longitudinal) L-direction, the transverse direction (TD) is parallel to the transverse (T) direction of the sheet material, and the normal direction (ND) is parallel to the thickness (S) direction of the sheet material.

The cross section of the Ti-6242 sheet reveals elongated grains with an average aspect ratio of  $0.50 \pm 0.10$ . The average length of the major axis of the  $\alpha$  grains is  $(4.4 \pm 1.3)$   $\mu\text{m}$ , and the corresponding average minor axis is  $(1.4 \pm 0.5)$   $\mu\text{m}$  (Fig. 5(a)). The grain shape orientation is defined as the angle between the major axis of an ellipse fit to a grain and the horizontal rolling direction RD. The grains of the base material did not exhibit any preferred grain shape orientation. Phase analysis using EBSD yielded a  $\beta$ -phase content of 5.9 % and  $\alpha$ -phase content of 94.1 %.

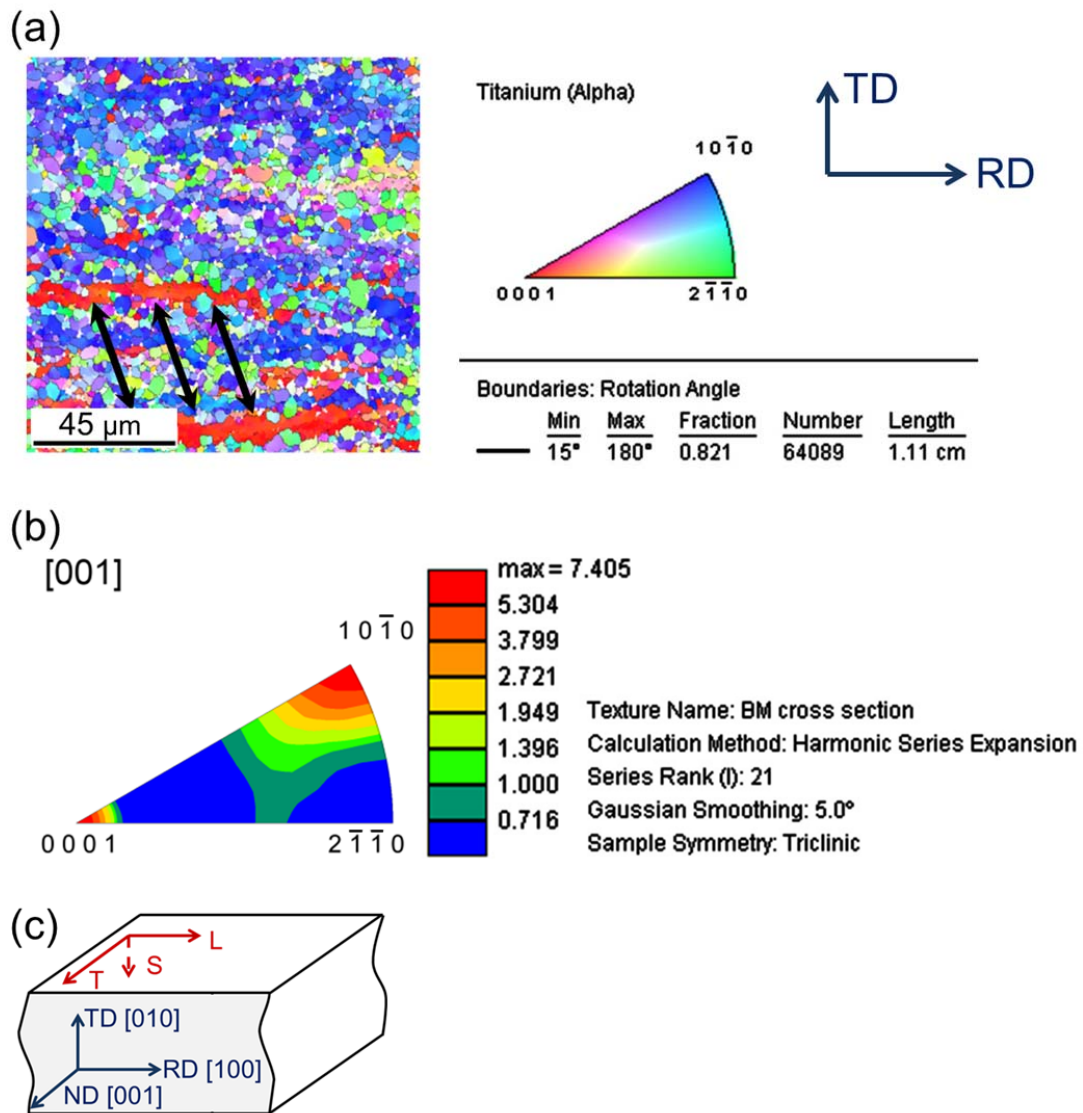


Fig. 5. Cross section of the Ti-6242 sheet: (a) crystal orientation map, (b) [001] inverse pole figure and (c) position of the coordinate system for the EBSD-analysis on the Ti-6242 sheet specimen. The inverse pole figure plane is the cross-section of the sheet material, the reference direction (RD) is parallel to the rolling (L) direction of the sheet, the transverse direction (TD) is parallel to the thickness (S) direction S of the BM specimen, and the normal direction (ND) is parallel to the T-direction of the sheet.

The common processing route to achieve a fully equiaxed microstructure of ( $\alpha + \beta$ ) titanium alloys runs through stages of homogenization in the  $\beta$  phase field, deformation, recrystallization and solution annealing in the ( $\alpha + \beta$ )-phase field (Lütjering & Williams, 2007). The presence of not fully recrystallized grains with red colouring in the crystal

orientation map (black arrows in Fig. 5(a)) indicates that the Ti-6242 sheet was mill-annealed and explains the appearance of an axial intensity at the  $\langle 0\ 0\ 0\ 1 \rangle // \text{ND}$  corner of the inverse [001] pole figure. These lamellar grains in the Ti-6242 base material are comparable with a Ti-6Al-4V microstructure obtained after the mill-anneal process, which is characterized by omission of the recrystallization step (Lütjering & Williams, 2007). The crystal orientation map of the Ti-6242 base material appears mainly blue (Fig. 5(a)). From this, it follows that a large number of grains are oriented in the  $\langle 1\ 0\ -1\ 0 \rangle // \text{ND}$  direction, which is confirmed by the [001] inverse pole figure showing a maximum axis intensity at the  $\langle 1\ 0\ -1\ 0 \rangle // \text{ND}$  corner (Fig. 5(b)). Furthermore, the axis intensity distribution shows a spreading into the  $\langle 0\ 0\ 0\ 1 \rangle // \text{ND}$  and  $\langle 2\ -1\ -1\ 0 \rangle // \text{ND}$  crystal directions (Fig. 5(b)), which explains the presence of purple, green and red coded grains in the crystal orientation map.

Fibre laser beam welding of the cross-rolled and mill-annealed Ti-6242 sheet led to significant local changes in the microstructure (Fig. 6(a)-(d)). A comparison of the microstructural characteristics between the BM, the HAZ and the FZ of butt joints welded at three different levels of the linear heat input is given in Table 3.

Table 3. Microstructural characteristics of the three laser beam-welded butt joints.

Region	$\beta$ -phase content [%]	$d_{min}$ [in]	$d_{max}$ [ax]	$d_{min}/d_{max}$	HV 0.3
BM	5.9	$1.4 \pm 0.5$	$4.4 \pm 1.3$	$0.5 \pm 0.1$	$328 \pm 9$
$P = 3.0\ \text{kW}, v = 5.0\ \text{m} / \text{min}, P / v = 36\ \text{kJ/m}$					
HAZ	16.3	$0.7\ 3\ 0.2$	$2.0\ 3\ 0.7$	$0.4\ 3\ 0.1$	
FZ	8.6	$1.2\ 3\ 6\ \text{k}$	$6.2\ 3\ 6\ \text{k}$	$0.3\ 3\ 0.2$	$430 \pm 13$
$P = 5.5\ \text{kW}, v = 2.0\ \text{m} / \text{min}, P / v = 165\ \text{kJ/m}$					
HAZ	13.7	$1.0\ 1\ 0.3$	$3.4\ 1\ 1.0$	$0.4\ 1\ 0.1$	
FZ	6.6	$1.1\ 1\ 0.3$	$6.3\ 1\ 1.9$	$0.3\ 1\ 0.2$	$418 \pm 12$

Notes:  $P$  – laser power,  $v$  – advance speed,  $d_{min}$  – minor grain axis,  $d_{max}$  – major grain axis.

The thermal cycle during the LBW of Ti-6242 and subsequent cooling resulted in a local transformation of the cross-rolled and mill-annealed condition of the Ti-6242 sheet into a microstructure with acicular crystals and embedded globular grains (Fig. 6(a)).

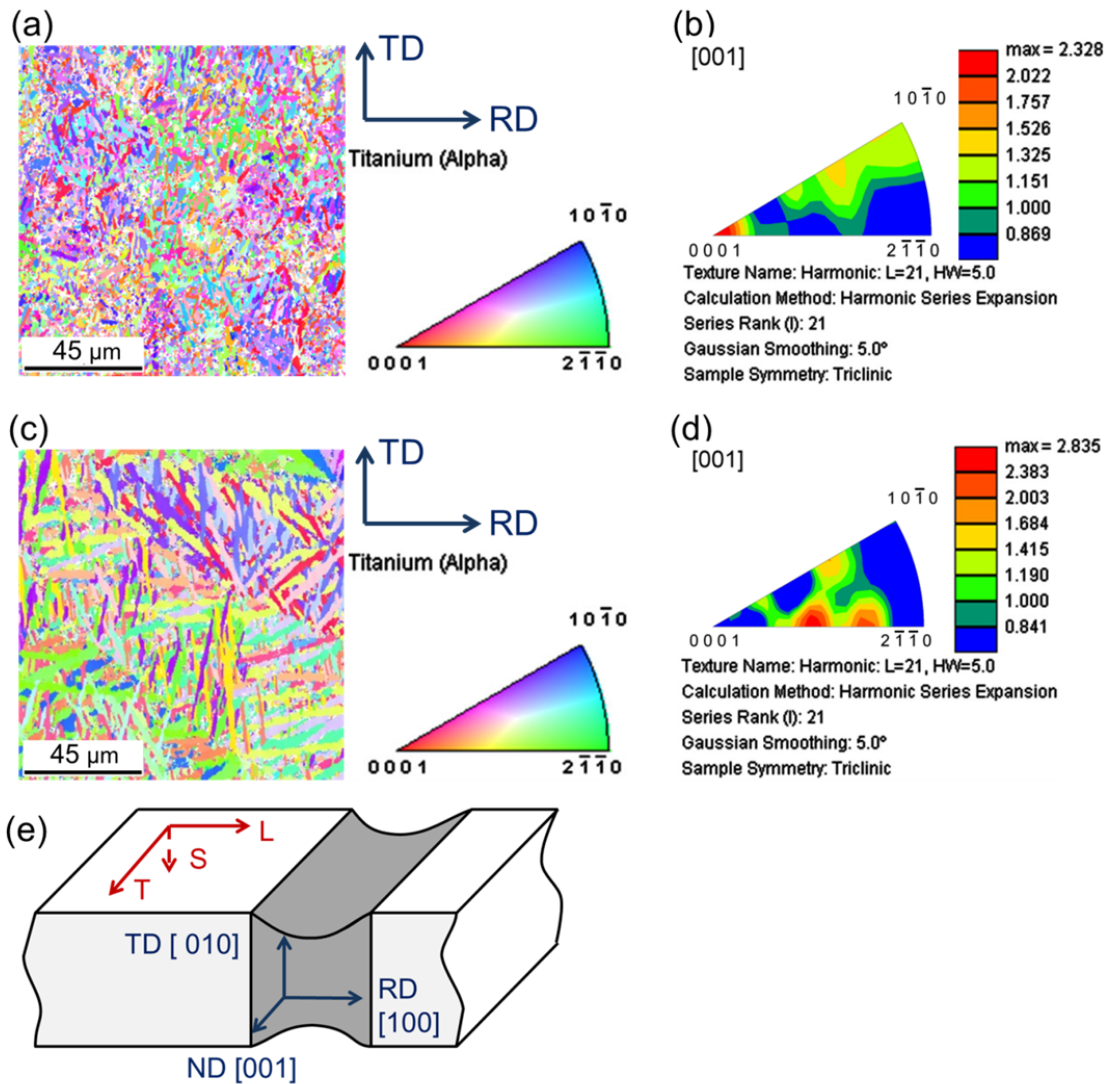


Fig. 6: Ti-6242 butt joint welded at 3.0 kW, 5.0 m/min, 36 kJ/m: (a) crystal orientation map of the HAZ and (b) corresponding [001] inverse pole figure; (c) crystal orientation map of the martensitic FZ and (d) corresponding [001] inverse pole figure. (e) Position of the coordinate system for the EBSD-analysis on the titanium sheet specimen. The pole figure plane is the cross-section of the sheet material, the reference direction (RD) is parallel to the rolling (L) direction of the sheet, the transverse direction (TD) is parallel to the thickness (S) direction S of the BM specimen, and the normal direction (ND) is parallel to the T-direction of the sheet.

The HAZ formation was associated with a grain refinement to an average grain size of  $2.0 \mu\text{m} \pm 0.7 \mu\text{m}$  for the major axis and  $0.7 \mu\text{m} \pm 0.2 \mu\text{m}$  for the minor axis when a grain is considered an ellipse, as well as an increase in the  $\beta$  content to 16.3% (Table 3). The present HAZ microstructure can be described as a mixture of martensitic  $\alpha'$  and primary  $\alpha$  and  $\beta$  phases. (Lütjering & Williams, 2007) assign the  $\beta$  transition temperature to  $995^\circ\text{C}$ . The higher  $\beta$  content within the HAZ adjacent to the FZ compared with the BM underlines the assumption that process temperatures were above the  $\beta$ -transus temperature of  $995^\circ\text{C}$ . (Orhan, et al., 2001), (Islam, et al., 1997) and (Salehi, et al., 1992) reported that the volume fraction of  $\beta$  phase increased with temperature for the Ti-6Al-4V alloy. It may be concluded that the HAZ development of the fibre laser beam welded Ti-6242 shows no other behaviour than that of Nd:YAG laser beam welded Ti-6Al-4V because the formation of acicular crystals requires temperatures higher than  $\beta$ -transus and subsequent rapid cooling from the  $\beta$  phase field to the  $(\alpha + \beta)$  phase (Kashaev, et al., 2015). Furthermore, the local microstructure transformation was associated with a change in the crystallographic single orientations. The recalculated [001] inverse pole figure (Fig. 5(b)) shows that the axis intensity of the  $\langle 1\ 0\ -1\ 0 \rangle // \text{ND}$  crystal direction is essentially lower compared with the BM, whereas the axis intensity at the  $\langle 0\ 0\ 0\ 1 \rangle // \text{ND}$ ,  $\langle 6\ 0\ -6\ 5 \rangle // \text{ND}$  and  $\langle 4\ 0\ -4\ 7 \rangle // \text{ND}$  increased. The splitting of the original  $\langle 1\ 0\ -1\ 0 \rangle // \text{ND}$  crystal direction means that the crystal rotations are connected with the morphological changes in the grains and  $\beta$  content during microstructure transformation.

The macroscopic FZ reveals a structure of columnar prior  $\beta$  grains heterogeneously grown from the HAZ in the opposite direction of the heat flux to the centreline after solidification (Fig. 1). The columnar prior  $\beta$  grains consist of an acicular  $\alpha'$  martensitic substructure with an average major axis length of  $(6.2 \pm 1.8) \mu\text{m}$  and minor axis length of  $(1.2 \pm 0.3) \mu\text{m}$  (Fig. 6(c)). The  $\beta$  content of 8.6% is lower compared with the HAZ. The present microstructure was formed by rapid cooling along the reaction path  $\beta \rightarrow (\alpha' + \beta)$ ,

whereas a diffusion-less transformation from the  $\beta$  phase to  $\alpha'$  martensite led to formation of a needle-like microstructure in the columnar prior  $\beta$  grains. The decrease in  $\beta$  content from 16.3% in the HAZ to 8.6% in the FZ is probably due to solution of  $\beta$  stabilizing Mo in the fine  $\alpha'$  plates. SEM investigations combined with EDX analysis yielded that the Mo concentration is almost equal both in the BM and FZ (Fig. 7(a) and (b), Table 4). (Ahmed & Rack, 1998) reported that a hexagonal  $\alpha'$  martensite formation in Ti-6Al-4V takes place at cooling rates higher than 410 °C/s. The resulting microstructure consists of long orthogonally oriented martensitic plates having an acicular morphology, a substructure containing dislocations and stacking faults and twins located in the platelets (Ahmed & Rack, 1998). Fig. 6(c) and Fig. 7(b) show a similar microstructure in the FZ of the laser beam welded Ti-6242. The crystal orientation map indicates that preferential orientations are not present, which is in contrast to the HAZ and BM. The corresponding recalculated [001] inverse pole figure shows maximums at  $\langle 2\ 2\ -4\ 5 \rangle // \text{ND}$ ,  $\langle 1\ 1\ -2\ 1 \rangle // \text{ND}$ ,  $\langle 0\ 6\ -6\ 5 \rangle // \text{ND}$  and  $\langle 0\ 1\ -1\ 3 \rangle // \text{ND}$  (Fig. 6(d)). This distribution explains the appearance of intermediate colours in the crystal orientation map and suggests that the fraction of pyramidal crystal planes is higher than that of the BM or the HAZ. The present microstructural characteristics of the FZ are similar to those for laser beam welded Ti-6Al-4V sheet (Kashaev, et al., 2016). The cooling rate within the HAZ adjacent to the FZ was sufficiently high to partially activate the diffusion-less  $\beta \rightarrow \alpha'$  transformation, which resulted in the formation of acicular crystals. Metallographic examinations reveal that the HAZ adjacent to the BM consisted of globular grains.

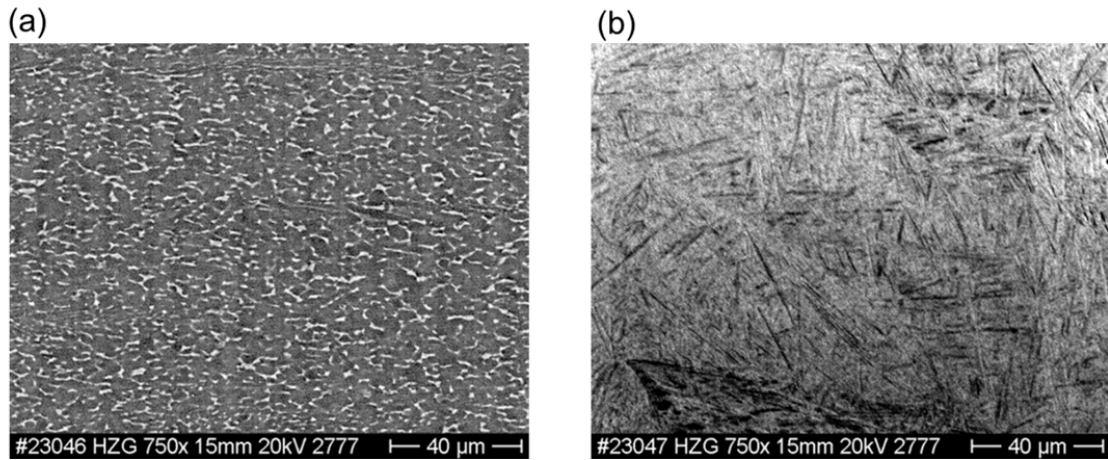


Fig. 7. BSE contrast of the different microstructures: (a) Ti-6242 BM, the  $\beta$  phase appears bright and (b)  $\alpha'$  martensitic FZ of a butt joint welded at 3.0 kW, 5.0 m/min, 36 kJ/m.

Table 4. Results of the EDX analysis (wt.%).

Region	Ti	Al	Sn	Zr	Mo
BM					
BM	88.22	5.11	1.77	3.50	1.39
$\alpha$ phase	89.09	5.80	-/-	3.45	1.67
$\beta$ phase	83.79	4.30	1.75	4.19	5.97
FZ ( $P = 5$ kW, $v = 6.2$ m / min, $P / v = 48.4$ kJ/m)					
RES	88.29	5.09	1.66	3.55	1.41
M	88.11	5.18	1.64	3.52	1.56
WRS	88.20	5.13	1.59	3.49	1.60

Notes: P – laser power, v – advance speed.

The increase in linear heat input from 36 kJ/m to 165 kJ/m caused an increase in the columnar prior  $\beta$  grain size, as well as an increase in the seam width (Fig. 1(a) and (b)). The reason is that a longer cooling time leads to more pronounced grain growth during solidification. Fig. 8 shows that microstructural properties of the HAZ and FZ of the Ti-6242 butt joint laser beam welded with 165 kJ/m are similar to those for the butt joint laser beam welded at 36 kJ/m. The comparison clearly demonstrates that the crystal

orientation is randomly distributed in the FZ both in the butt joint produced at 36 kJ/m and 165 kJ/m.

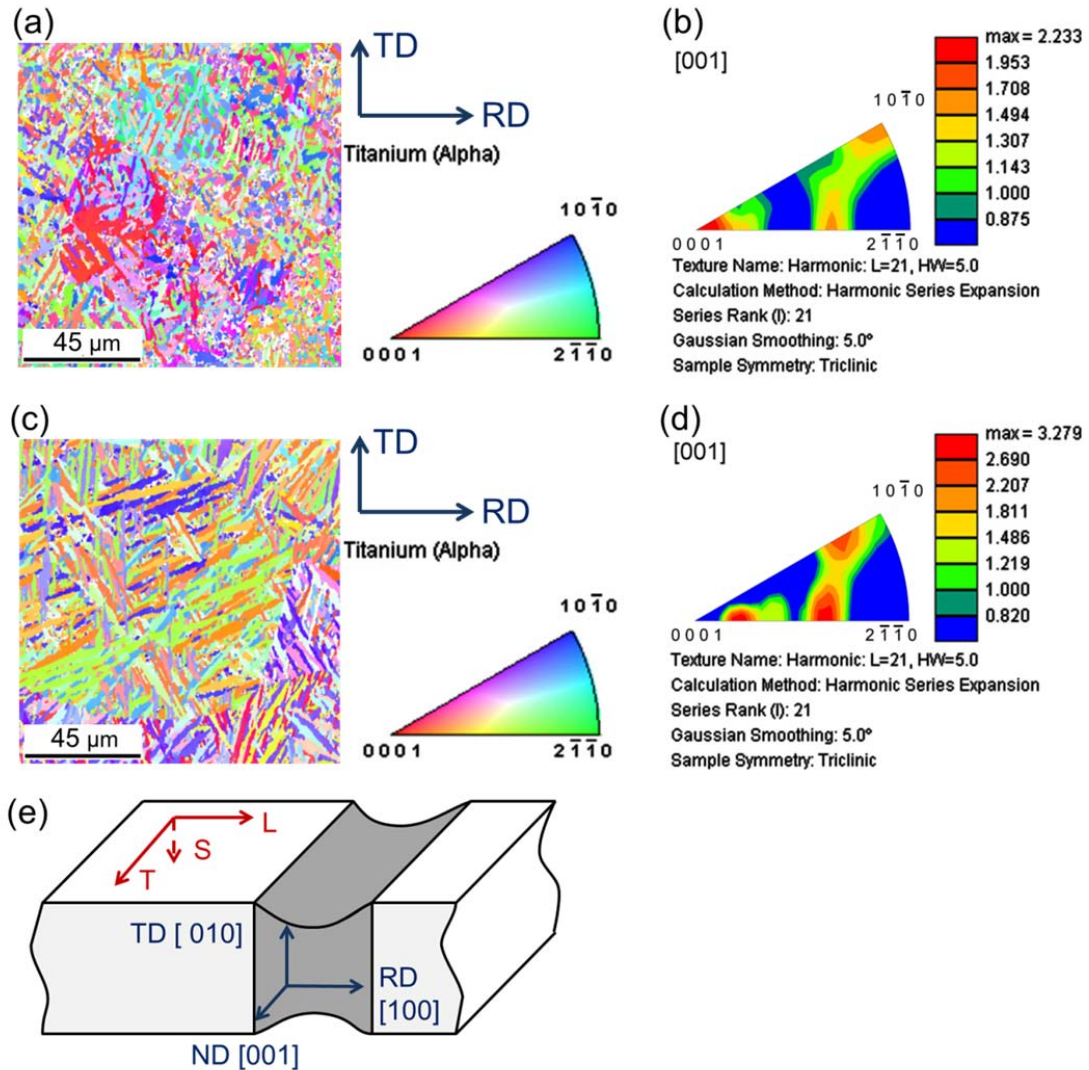


Fig. 8. Ti-6242 butt joint welded at 5.5 kW, 2.0 m/min, 165 kJ/m: (a) crystal orientation map of the HAZ and (b) corresponding [001] inverse pole figure, (c) crystal orientation map of the martensitic FZ and (d) corresponding [001] inverse pole figure. (e) Position of the coordinate system for the EBSD-analysis on the titanium sheet specimen. The inverse pole figure plane is the cross-section of the sheet material, the reference direction (RD) is parallel to the rolling (L) direction of the sheet, the transverse direction (TD) is parallel to

the thickness (S) direction S of the BM specimen, and the normal direction (ND) is parallel to the T-direction of the sheet.

Microhardness profiles were determined across the weld in three regions of the cross-section: the RES, middle and WRS, as shown in Fig. 9. The average microhardness values for the BM and FZs of the specimens welded at two different linear heat inputs are summarized in Table 3. The three measured microhardness profiles are close together for both specimens welded at a linear heat input of 36 kJ/m (Fig. 9(a)) and welded at a linear heat input of 165 kJ/m (Fig. 9(b)). The indentation within the BM was mainly parallel to the  $\langle 1\ 0\ -1\ 0 \rangle$ //ND crystal direction. The continuous increase in hardness within the HAZ from the BM to the FZ is due to the increasing amount of martensitic  $\alpha'$  phase. The martensitic  $\alpha'$  phase provides high strength and hardness accompanied by a loss of ductility and toughness, due to the formation of a substructure containing dislocations, stacking faults and twins located in the platelets, as reported by (Ahmed & Rack, 1998), as well as an enforced solution of the  $\beta$  stabilizing alloying element Mo in the  $\alpha'$  phase. The effect of the  $\langle 0\ 0\ 0\ 1 \rangle$ //ND crystal direction accumulated at a higher level in the HAZ adjacent to the FZ cannot be excluded. The specimen welded at the highest linear heat input of 165 kJ/m exhibits a slightly lower average microhardness in the FZ compared with the two specimens welded at lower linear heat input levels (Table 3). This response may be attributed to the different average prior  $\beta$  grain sizes, i.e., the Hall–Petch mechanism. As mentioned above, the average grain size in the FZ of the specimens welded at lower heat input levels is smaller than that of the specimens welded at the highest linear heat input of 165 kJ/m.

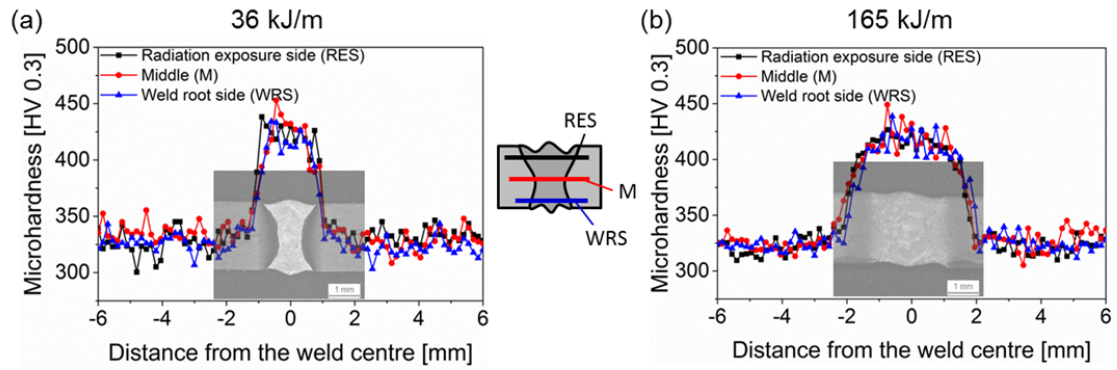


Fig. 9. Microhardness profiles of the (a) specimen welded at 36 kJ/m and (b) the specimen welded at 165 kJ/m.

### 3.2 Tensile strength

The results of the tensile tests are shown in Table 5. As expected from the microstructure (Fig. 5), the Ti-6242 sheet shows a dependence on the test direction due to the anisotropy of the hcp  $\alpha$ -phase. The mechanical behaviour of Ti alloys under tensile load is determined by their dependence on their grain orientation due to the low symmetry of the hexagonal  $\alpha$ -phase, as reported by (Deka, et al., 2006), which is the majority phase for Ti-6242. Individual slip systems such as the  $\{0\ 0\ 0\ 1\}\langle 1\ 1\ -2\ 0\rangle$ ,  $\{1\ 0\ -1\ 0\}\langle 1\ 1\ -2\ 0\rangle$ ,  $\{1\ 0\ -1\ 1\}\langle 1\ 1\ -2\ 0\rangle$  ( $\langle a \rangle$  type slip on basal, prismatic or pyramidal planes) as well as the  $\{1\ 0\ -1\ 1\}\langle 1\ 1\ -2\ 3\rangle$  (pyramidal  $\langle c + a \rangle$  type 1<sup>st</sup> order) and  $\{1\ 1\ -2\ 2\}\langle 1\ 1\ -2\ 3\rangle$  (pyramidal  $\langle c + a \rangle$  type 2<sup>nd</sup> order) are characterized by differences in deformation resistance, which is the main reason for the high anisotropy of the hcp  $\alpha$ -phase, as reported by (Deka, et al., 2006). Grains with their  $\langle 0\ 0\ 0\ 1 \rangle$  crystal orientation close to the deformation axis arranged according to  $\langle c + a \rangle$  are significantly stronger than other grains because the  $\langle c + a \rangle$  dislocation slip needs a much higher critical resolved shear strength (CRSS) than the  $\langle a \rangle$  type slip, as reported by (Deka, et al., 2006). As already shown in Fig. 4(a), the (0 0 0 2) pole figure of the Ti-6242 BM exhibits basal poles with high intensities along the transverse direction TD, a spread angle of approximately  $40^\circ$ , and basal poles of lower intensities along the rolling direction RD with a wide spread angle of approximately  $80^\circ$ . From this, it follows that the amount of grains needing a lower CRSS for  $\langle c + a \rangle$  type slip on the pyramidal planes is higher in the longitudinal direction RD than in the

transversal TD for the Ti-6242 sheet. The performed tensile load tests confirm that the strength is higher in the TL direction compared with the LT direction.

The laser beam welded Ti-6242 butt joint fractured within the BM. The condition of the HAZs and laser beam weld did not influence globally the mechanical behaviour of the butt joint when subjected to a static tensile load due to its higher strength compared with the BM. Due to the strength mismatch of the laser beam welds, as indicated by the microhardness measurements (Fig. 9), the main specimen deformation occurred in the BM. This is explained by a decrease in the fracture strain, which was determined by taking the entire gauge length into account and a non-plastically deformed weld region.

Table 5. Tensile test results. Average values with standard deviations were calculated from three measured values.

<b>Specimen</b>	<b>R<sub>p0.2</sub></b> <b>[MPa]</b>	<b>R<sub>m</sub></b> <b>[MPa]</b>	<b>A</b> <b>[%]</b>
<b>BM LT</b>	972 ± 9	1016 ± 9	15 ± 0.4
<b>BM TL</b>	1013 ± 3	1077 ± 2	15 ± 0.4
<b>LBW</b> <b>(specimen welded at 5</b> <b>kW laser power and</b> <b>5 m / min advance</b> <b>speed)</b>	993 ± 1	1033 ± 2	13 ± 1.0

Notes: “LT”– loading in the longitudinal direction of the sheet, “TL”– loading in the transverse direction of the sheet.

### 3.3. Effect of weld imperfections on tensile strength

From an industrial point of view, high-performance welding processes must be implemented at high advance speeds. The main disadvantage of using high advance speeds at high laser powers during autogenous LBW is the formation of underfills, as is clearly seen in a cross-section of the butt joint (Fig. 3(a)). For LBW at 8 kW laser power combined with an 8 m/min advance speed, the total underfill,  $UF$  (Fig. 3(b)), is 0.39 mm (Fig. 3(a)). This is 19.5% of the specimen thickness. The presence of underfill or undercut decreases the cross-sectional thickness of the weld and can therefore decrease the tensile strength of the weld. According to American National Standard AWS D17.1 (D17.1, 2012), the maximum allowable underfill depth is 7% of a specimen thickness. To investigate the influence of the underfill depth on the tensile strength of the welds, a FE-model of the tensile behaviour of the specimens with different underfill depths was performed.

To predict the macroscopic stress-strain behaviour of a tensile specimen with a weld, a 3D FE-model with two-plane-symmetry reduced to a quarter of the tensile specimen was generated (Fig. 10). The FEM mesh consisted of 24064 quadrilateral elements (C3D8R) with finer elements located in the weld zone: 16 elements through the thickness ( $z$ ), 20 elements normal to the loading direction ( $y$ ) and 12 elements parallel to the loading direction. The discretisation in the loading direction within the BM gauge length was approx. 0.25 mm. A total of 15 FE-models were created with the different total underfill depths from  $UF = 0.0$  (weld seam without underfill/undercut) to  $UF = 1.0$  mm. The weld seam width was kept constant at 1.65 mm for all of the FE-models. Nonlinear isotropic hardening and large deformation theory were used. Isotropic material behaviour was assumed for the two zones in the model: the BM and the weld zone. The nonlinear stress-strain behaviour for the BM and the weld was defined in ABAQUS using piecewise linear segments for the true stress-true plastic strain behaviour.

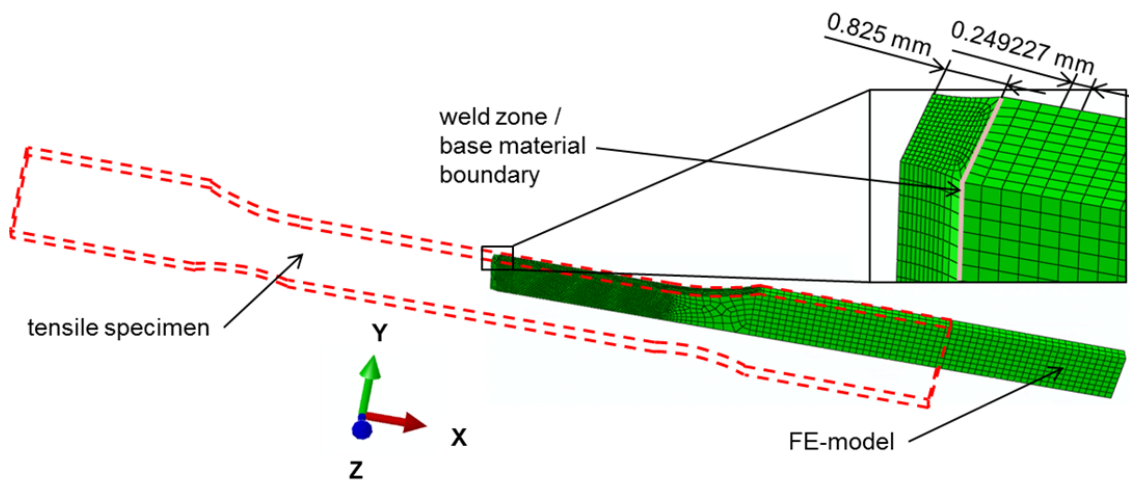


Fig. 10. FE-model of the tensile specimen with a weld seam.

The material properties in the weld seam were determined by an instrumented indentation testing procedure for the local stress-strain properties, as described by (Rao, et al., 2013). This procedure is based on the force–depth curve analyses via artificial neural networks to derive local stress–strain curves. Using the indentation procedure for the FZ of the investigated specimen, the values for the Young’s modulus,  $E$ , yield strength,  $R_{p\ 0.2}$ , and ultimate tensile strength (UTS),  $R_m$  were identified, as listed in Table 6.

The value for the Young’s modulus obtained through the instrumented indentation test (87.4 GPa) was lower than the value obtained via tensile testing (112.0 GPa). Therefore, the Young’s modulus for the weld,  $E_W$ , was proportionally estimated according to the following equation:

$$E_W = E_{W\ II} \times E_{BM\ TT} / E_{BM\ II}, \quad (2)$$

where  $E_{W\ II}$ ,  $E_{BM\ TT}$  and  $E_{BM\ II}$  are the Young’s modulus values for the weld obtained through the instrumented indentation test, for the BM obtained from the tensile test and

for the BM from the instrumented indentation test, respectively. Based on similar assumptions, the yield strength for the weld,  $R_{p\ 0.2\ W}$ , was determined from:

$$R_{p\ 0.2\ W} = R_{p\ 0.2\ W\ II} \times R_{p\ 0.2\ BM\ TT} / R_{p\ 0.2\ BM\ II}, \quad (3)$$

where  $R_{p\ 0.2\ W\ II}$ ,  $R_{p\ 0.2\ BM\ TT}$ , and  $R_{p\ 0.2\ BM\ II}$  are the values for the yield strength of the weld obtained from the instrumented indentation test, for the BM via the tensile test and for the BM from the instrumented indentation test, respectively. The maximum stress value in the elastic region for the weld,  $R_{elastic\ W}$ , was estimated from the value for the BM obtained via tensile testing,  $R_{elastic\ BM\ TT}$ , according to the equation:

$$R_{elastic\ W} = R_{elastic\ BM\ TT} \times R_{p\ 0.2\ W} / R_{p\ 0.2\ BM\ TT}. \quad (4)$$

The ultimate tensile strength for the weld of 2082 MPa obtained through the instrumented indentation test was overestimated (Table 6). The value for the weld  $R_{m\ W}$  was calculated based on an assumption that there was a linear correlation between the hardness and ultimate tensile strength, which is well known for steel and holds for Ti alloys (Murakami, 2002):

$$R_{m\ W} = R_{m\ BM\ TT} \times HV_{FZ} / HV_{BM} = 1313 \text{ [MPa]}, \quad (5)$$

where  $R_{m\ BM\ TT}$ ,  $HV_{FZ}$  and  $HV_{BM}$  are the UTS for the BM obtained via the tensile test, the average microhardness of FZ (424 HV 0.3) and the average microhardness of the BM (328 HV 0.3), respectively.

Table 6. Mechanical properties obtained via the instrumented indentation test, tensile test and calculated values for the weld seam used to determine the stress-strain behaviour. Butt joint welded at 3.0 kW, 5.0 m/min, 36 kJ/m.

	<b>E [GPa]</b>	<b>R<sub>elastic max</sub></b>	<b>R<sub>p 0.2</sub> [MPa]</b>	<b>R<sub>m</sub> [MPa]</b>
<b>Average values obtained through the instrumented indentation test</b>				

<b>BM</b>	87.4	-	1070	1436
<b>weld</b>	100.1	-	1250	2082
<b>Average values obtained through the tensile test</b>				
<b>BM</b>	112.0	810.1	972	1016
<b>Proportional estimation</b>				
<b>weld calculated</b>	128.3	946.0	1135	1313

The true stress vs. true strain material data for the BM were calculated from an average stress-strain-curve obtained in the TL-direction. The maximum value for the true stress of 810.1 MPa for the elastic region for the BM was identified at a true strain value of 0.00703. Assuming that for the weld the values for  $R_{elastic\ max}$ ,  $R_{p\ 0.2}$ , and  $R_m$  will occur at the same strain values as for the BM, three points on the true stress-true plastic strain curve for the weld were determined. A non-linear regression with a power function based on the three values was performed:

$$\sigma = A\varepsilon^P, \quad (6)$$

where  $\sigma$  and  $\varepsilon$  are the true stress and true plastic strain, respectively. The constants  $A = 1491$  MPa and  $P = 0.03895$  for the nonlinear regression were determined using the least squares method. Equation (6) was used to calculate the stress values for the true stress-true plastic strain behaviour of the weld. The plastic true stress-true strain curves for the BM and the weld used for the modelling work are shown in Fig. 11.

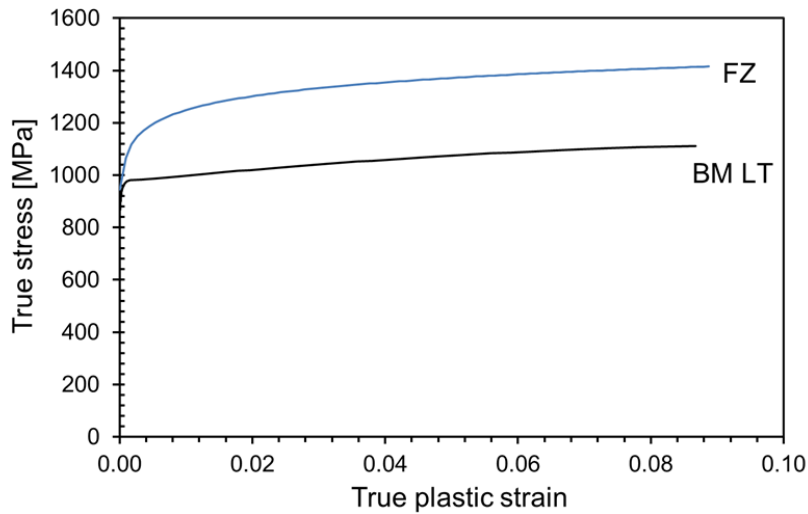


Fig. 11. True stress-plastic strain curves used for modelling of the tensile behaviour of the specimens with welded butt joints.

Fig. 12 shows the tensile specimen with the weld after tensile testing and the strain map calculated in ABAQUS. The maximum strain was determined to be in the BM outside the weld where tensile fracture occurred. The figure shows that the modelling results are in good agreement with the experimental results. The engineering stress-strain curves (both the experimental and calculated curve based on the FE-modelling results) for specimens with a weld seam having different underfill depths are represented in Fig. 13. The results show that the predicted stress-strain curves are in good agreement with the experimental stress-strain curve for the specimen with a weld up to the ultimate strain. The stress-strain behaviour for the higher strain ranges cannot be predicted with high accuracy. However, based on the modelling results, the behaviour in the elastic and the plastic-region up to the UTS can be predicted with high accuracy. The difference between the predicted values and those obtained from tensile testing for the UTS and the strain at UTS are 1.2% and 4.4%, respectively. The results show that for the investigated specimen geometry, the critical underfill value where a reduction in the UTS occurs is approximately 0.5 mm, which is 25% of the specimen thickness. The predicted values for the UTS and the strain at UTS are shown in Fig. 13(b). We conclude that during LBW, for structures with a thickness of 2 mm, the total underfill value can be no greater than 0.5 mm to ensure no decrease in the static strength due to the welding process.

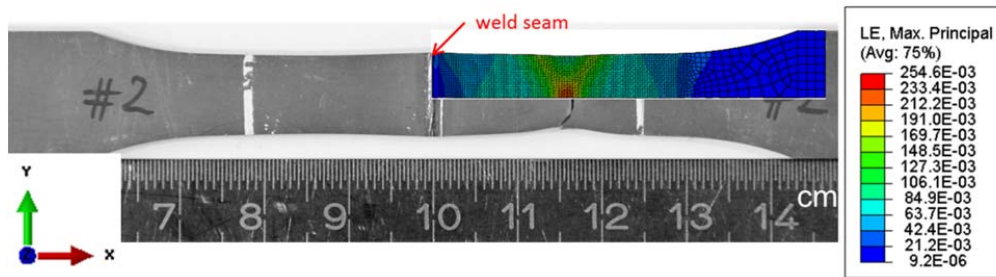


Fig. 12. Photo of a specimen after tensile testing over-plotted with a logarithmic strain map calculated using ABAQUS.

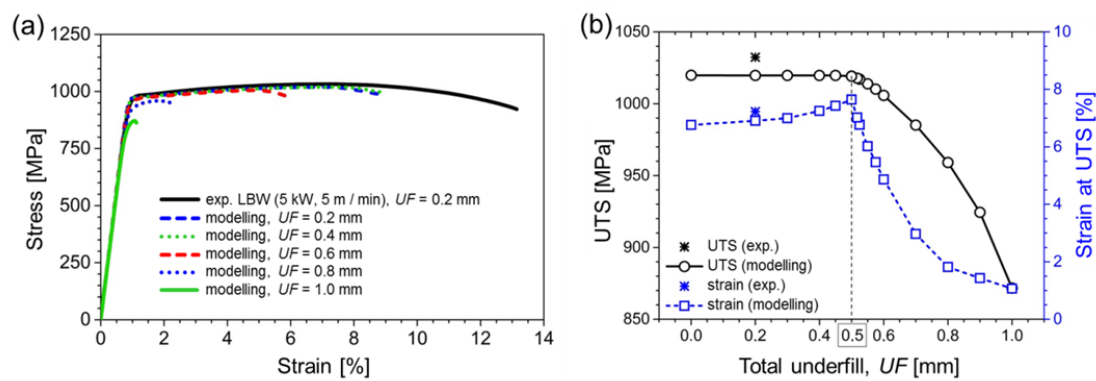


Fig. 13. (a) Modelling and experimental results for the tensile test behaviour of the specimens with butt-joints containing different total underfill values and (b) UTS and strain at UTS vs. the total underfill depth (both modelling and experimental results shown).

#### 4. Conclusion

(1) Autogenous LBW of Ti-6242 butt joints was performed to investigate the morphological and geometric characteristics of the weld. Welds with a low level of porosity and an appropriate seam geometry were obtained.

(2) The laser beam welded Ti-6242 butt joint consisted of a martensitic FZ and an inhomogeneous HAZ. The HAZ adjacent to the BM consisted of globular grains. This microstructure changed to a mixture of  $\alpha$ -phase, martensitic  $\alpha'$ -phase and  $\beta$ -phase. The thermal cycling changed the average grain size,  $\beta$ -phase content and micro-texture of the welds.

(3) The microhardness profiles exhibited a continuous increase within the HAZ from the BM to the FZ due to the increasing amount of martensitic  $\alpha'$ -phase.

(4) The mechanical behaviour of the LBW Ti-6242 butt joints in tension was dominated by the properties of the Ti-6242 BM, despite the presence of geometrical notches in the samples. The local increases in hardness provide a shielding effect and protected the Ti-6242 butt joint from mechanical damage. The predicted critical total underfill depth that reduces the tensile strength of the weld is determined to be 25% of the specimen thickness.

### **Acknowledgements**

The authors would like to thank Mr. R. Dinse, Mr. P. Haack and Mr. F. Dorn from Helmholtz-Zentrum Geesthacht for their valuable technical support.

### **References**

- Ahmed, T. & Rack, H., 1998. Phase transformation during cooling in  $\alpha + \beta$  titanium alloys. *Mater. Sci. Eng. A243*, pp. 206-2011.
- Baerlack III, W. & Banas, C., 1981. A comparative evaluation of laser and gas tungsten arc weldments in high-temperature titanium alloys. *Welding research supplement*, pp. 121-130.
- Cao, X. et al., 2014. Global and local mechanical properties of autogenously laser welded Ti-6Al-4V. *Metall. Mater. Trans. A 45A*, pp. 1258-1272.
- Chamanfar, A., Pasang, T., Ventura, A. & Misiolek, W., 2016. Mechanical properties and microstructure of laser welded Ti-6Al-2Sn-4Zr-2Mo (Ti6242) titanium alloy. *Mater. Sci. Eng. A 663*, pp. 213-224.
- D17.1, A., 2012. *Specification for fusion welding for aerospace applications (2nd ed.)*, Miami, FL, USA: American Welding Society (AWS) D17 Committee on Welding in the Aircraft and Aerospace Industries.
- Davis, J., 1997. Properties of nonferrous heat-resistant materials. In: A. International, Hrsg. *Heat-resistant Materials*. Materials Park, USA: s.n., pp. 345-438.

- Deka, D., Joseph, D., Ghosh, S. & Mills, M., 2006. Crystal plasticity modelling of deformation and creep in polycrystalline Ti-6242. *Metall. Mater. Trans. A* 37, pp. 1371-1388.
- Islam, M., Pillin, J. & Ridley, N., 1997. Effect of surface finish and sheet thickness on isostatic diffusion bonding of superplastic Ti-6Al-4V. *Mater. Sci. Tech.* 13(12), pp. 1045-1050.
- Kashaev, N., Pugachev, D., Riekehr, S. & Ventzke, V., 2016. Fiber laser beam welding of Ti-6242 – Effect of processing parameters on microstructural and mechanical properties. *Mater. Sci. Forum* 879, pp. 903-908.
- Kashaev, N. et al., 2016. Effect of Nd:YAG laser beam welding on weld morphology and mechanical properties of Ti-6Al-4V butt joints and T-joints. *Opt. Lasers. Eng.* 86, pp. 172-180.
- Kashaev, N. et al., 2015. Microstructure and mechanical properties of laser beam welded joints between fine grained and standard Ti-6Al-4V sheets subjected to superplastic forming. *Adv. Eng. Mater.* 17(3), pp. 374-382.
- Lütjering, G. & Williams, J., 2007. Alpha + beta alloys. In: Springer, Hrsg. *Titanium 2nd ed.*. Berlin, Heidelberg, New York: s.n., pp. 203-258.
- Lütjering, G. & Williams, J., 2007. High temperature alloys. In: Springer, Hrsg. *Titanium 2nd ed.*. Berlin, Heidelberg, New York: s.n., pp. 259-282.
- Murakami, Y., 2002. *Metal Fatigue: Effects of Small Defects and Nonmetallic Inclusions*. Oxford, UK: Elsevier Science Ltd..
- Orhan, N., Khan, T. & Eroglu, M., 2001. Diffusion bonding of a microduplex stainless steel to Ti-6Al-4V. *Scripta Mater.* 45, pp. 441-446.
- Rao, D. et al., 2013. Asymmetric mechanical properties and tensile behaviour prediction of aluminium alloy 5083 friction stir welding joints. *Mater. Sci. Eng. A565*, pp. 44-50.
- Salehi, M., Pilling, J., Ridley, N. & Hamilton, D., 1992. Isostatic diffusion bonding of superplastic Ti-6Al-4V. *Mater. Sci. Eng. A150*, pp. 1-6.

- Squillace, A., Prisco, U., Ciliberto, S. & Astarita, A., 2012. Effect of welding parameters on morphology and mechanical properties of Ti-6Al-4V laser beam welded butt joints. *J. Mater. Process. Technol.* 212, pp. 427-436.
- Torster, F., dos Santos, J., Kocak, M. & Penasa, M., 1999. Mechanical and microstructural characterization of laser beam welded titanium alloys. In: A. International, ed. *Proc. 5th International Conference on Trends in Welding Research*. Materials Park, Ohio, USA: s.n., pp. 887-892.
- Wood, J., Russo, P., Welter, M. & Crist, E., 1998. Thermomechanical processing and heat treatment of Ti-6Al-2Sn-2Zr-2Cr-2Mo-Si for structural applications. *Mater. Sci. Eng. A* 243(1,2), pp. 109-118.